Effect of zirconia on Pd–Pt supported SBA-15 catalysts for the oxidation of methane

Caravaggio, Gianni; Nossova, Lioudmila; Turnbull, Matthew

Publisher's version / Version de l'éditeur:
https://doi.org/10.3390/catal13060926
Catalysts, 13, 6, 2023-05-24

catalysts

MDPI

Article

Effect of Zirconia on Pd–Pt Supported SBA-15 Catalysts for the Oxidation of Methane

Gianni Caravaggio [1,*], Lioudmila Nossova [1] and Matthew Turnbull [2]

[1] Natural Resources Canada (NRCan), CanmetENERGY—Ottawa, 1 Haanel Drive, Ottawa, ON K1A 0R6, Canada
[2] National Research Council Canada, 1200 Montreal Road, Ottawa, ON K1A 0R6, Canada
* Correspondence: gianni.caravaggio@nrcan-rncan.gc.ca

Abstract: A series of methane oxidation catalysts were prepared by doping Santa Barbara Amorphous-15 (SBA-15), a highly mesoporous silica sieve, with varying amounts of Zr (5, 10, and 15 wt%) and loading with 2 wt% Pd and 4 wt% Pt. The catalysts were characterized using various techniques, including BET, X-ray diffraction (XRD), X-ray photoelectron spectroscopy (XPS), and H_2-temperature programmed reduction (H_2-TPR). Fresh and aged catalysts were evaluated for methane oxidation. Aging was performed using a simulated lean burn natural gas (NG) engine exhaust containing water vapor (10% vol) and sulfur (10 ppm). It was found that the catalyst with 15 wt% zirconia was the most active and stable of the series, exhibiting the lowest T_{50} of 481 °C after 40 h of aging. The Pd–Pt catalyst loaded on pure SBA-15 had a T_{50} of 583 °C after aging, which was 102 °C higher than that of the Pd–Pt catalyst with 15 wt% Zr. The results suggest that the increased performance was due to the higher amount of reducible PtO_x species in the proximity of ZrO_2 and the sulfur scavenging effect of zirconia, which protected the active metals from forming inactive sulfur complexes. Overall, the Pd–Pt catalyst with 15 wt% Zr loaded on SBA-15 demonstrated excellent methane oxidation activity, hydrothermal stability, and sulfur resistance and can be considered a viable candidate for reducing the methane slip from a lean burn NG engine exhaust.

Keywords: catalytic oxidation of methane; methane slip; natural gas engine; palladium; platinum catalyst

Citation: Caravaggio, G.; Nossova, L.; Turnbull, M. Effect of Zirconia on Pd–Pt Supported SBA-15 Catalysts for the Oxidation of Methane. *Catalysts* **2023**, *13*, 926. https://doi.org/10.3390/catal13060926

Academic Editors: Leonarda Liotta and Kevin J. Smith

Received: 21 February 2023
Revised: 18 April 2023
Accepted: 4 May 2023
Published: 24 May 2023

1. Introduction

Natural gas (NG) has been considered a fuel of choice in the transition toward a zero-carbon economy in the heavy-duty (lean burn engine) segment. It is abundant, inexpensive, and produces approximately 20–25% less greenhouse gas (GHG) on a life-cycle basis than diesel and gasoline engines. Lean burn NG engines are similar in performance to diesel engines, but they produce high levels of unburned methane (also called methane slip) in the exhaust. Methane requires a higher temperature to achieve combustion than conventional fuels; thus, cold spots or dead volume in an engine cylinder lead to incomplete combustion [1]. The unburned methane needs to be eliminated because it is a potent GHG (~86 GHG impact compared to CO_2 for 20 years after emission) and can negate the benefit of the NG engine [2]. Methane is difficult to oxidize, since the molecule's strong C-H bonds make it highly stable, which prevents low-temperature oxidation and requires a temperature of more than 1000 °C for complete combustion [3]. Catalytic combustion is considered to be an effective method to reduce methane emissions at low temperatures, and Pd-based catalysts are well known to be highly effective for oxidizing methane under lean burn and low-temperature conditions [4–10]. Despite the superior activity of these catalysts, they are prone to water inhibition and sulfur poisoning [4,11]. As such, they are not very effective at eliminating methane slip during long-term usage under real conditions since sulfur and water are present in the exhaust of lean burn NG vehicles (NGVs).

It is hypothesized that water inhibition for these catalysts is due to the formation of stable $Pd(OH)_2$ groups and/or blocking of the O interchange between the support and Pd active sites by OH groups [12]. Various researchers have identified that catalysts of Pd on amorphous silica [13] or on zeolite with high silica content [14] used for methane oxidation conferred hydrothermal stability due to silica's hydrophobic nature. Therefore, it would be of interest to explore other types of hydrophobic supports, such as mesoporous silica, to prepare methane oxidation catalysts. In comparison to other silicas, SBA-15 was shown to be a desirable support to load palladium nanoparticles because its unique combination of pore size, pore structure (2D hexagonal), and thick pore walls limits the sintering of metal particles [15].

The presence of water in the exhaust feed is not the only reason for the deactivation of the catalyst. The reaction of SO_2 with Pd, which is known as sulfur poisoning, produces inactive palladium sulfur oxide species ($Pd(SO_x)$), which significantly decreases the overall catalytic activity of the catalyst [11]. Various researchers have found that adding Pt or Zr to Pd-containing catalysts improved the sulfur tolerance of the material. For example, Corro et al. established that Pt(0), in a reduced Pd–Pt/Al_2O_3 catalyst, reacted more quickly with SO_2 than Pd, freeing the Pd to react with methane [11]. Another recent study proposed that adding Pt would improve the activity of a Pd-modified Mn-hexaaluminate catalyst for the oxidation of methane, even in the presence of SO_2 and water [16]. The authors related the improved water and sulfur resistance to the presence of Pt–Pd alloy particles.

Venezia et al. [17] found that a mesoporous SBA-15-supported Pd catalyst with 10% wt% TiO_2 added to the SBA-15 significantly improved the catalyst activity and sulfur tolerance compared to Pd loaded on SBA-15 alone. The increased sulfur tolerance was attributed to the scavenging effect of TiO_2 on SO_2, thus allowing Pd to stay unchanged for the reaction with methane. However, the addition of titania to silica increased the acidity of the support. As a result, the scavenger action of titania could be substantially decreased due to the stronger water adsorption on the acidic sites. For that reason, it would be interesting to modify the catalyst with more basic zirconia, which would interact much stronger with SO_2 molecules. Escandon et al. [18] showed higher sulfur resistance of Pd supported on zirconia; however, zirconia provides much less surface area for dispersion of active metals compared to alumina or silica. Therefore, in summary, we can expect a synergetic effect for enhanced catalytic performance by using a combination of Pd active metal with Pt supported on high surface area silica (SBA-15), which is promoted by zirconia.

The objective of this study was to develop a novel methane oxidation catalyst with hydrothermal stability and sulfur-resistant properties by adding Zr to Pd/Pt/SBA-15 catalyst. To this aim, mesoporous SBA-15 was modified by the addition of Zr (5, 10, and 15 wt%) followed by loading with 2 wt% Pd and 4 wt% Pt. We used a relatively high content of Pd and Pt (total, 6 wt%) despite the current trend of lowering the cost of catalysts by reducing the amount of precious metals. This was done to ensure that sufficient methane conversion and stability would be achieved under typical lean burn NGV exhaust conditions, that contain water vapor, sulfur compounds, and temperatures of 250–600 °C. Velin et al. [19], for example, showed that a catalyst required at least 3.6 wt% Pd on alumina to achieve a T_{50} near 400 °C in a feed that contained water without sulfur, which also negatively affects catalyst activity.

The catalysts were characterized using various techniques (BET, XRD, TPR, XPS) to establish a correlation between the physico-chemical properties of the materials and their performance in the complete oxidation of methane. Fresh and aged catalysts were tested for methane oxidation activity under conditions with the same simulated NGV exhaust that contained water vapor and sulfur in the stream.

2. Results and Discussions

2.1. SEM-EDX and FAA

The catalyst compositions were determined by FAA and SEM-EDX methods. Table 1 shows the comparison of their experimental composition in wt% and nominal values. The data show that the amounts of main components of calcined materials were very close to the intended nominal values for most elements. A few results differ from the nominal values by approximately 25% but are still close enough to indicate that the metals were loaded onto the SBA-15 in the intended amounts.

Table 1. Nominal, SEM-EDX, and FAA wt% values of 2Pd/4Pt/xZr/SBA-15 catalysts.

Nominal wt%	Pd [a]	Pt [a]	Zr [b]
2Pd/4Pt	2.0	4.2	NA
2Pd/4Pt/5Zr	2.1	3.3	5.4
2Pd/4Pt/10Zr	1.9	3.2	9.3
2Pd/4Pt/15Zr	1.9	3.1	12.0

[a] FAA analysis; [b] SEM-EDX analysis; NA—not applicable.

2.2. Textural Characterization

The adsorption/desorption isotherms of pure SBA-15 support, and the catalysts loaded with Pd, Pt, and zirconia are shown in Figure 1. The isotherm of SBA-15 was typical for samples with type IVa mesoporous materials and some micropores according to the IUPAC classification. The catalysts also demonstrated type IVa mesoporous material isotherms, indicating that loading the metals did not destroy the mesoporous structure of SBA-15 [20]. The hysteresis loops presented H1 types, indicating mesoporous materials with tube-shaped channels open at both ends [21].

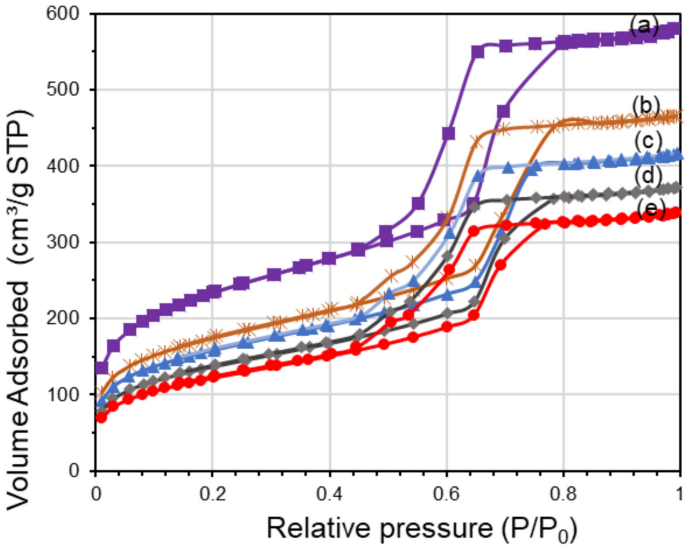

Figure 1. N_2 adsorption and desorption isotherms of: (**a**) SBA-15, (**b**) 2Pd/4Pt/SBA-15, (**c**) 2Pd/4Pt/5Zr/SBA-15, (**d**) 2Pd/4Pt/10Zr/SBA-15, and (**e**) 2Pd/4Pt/15Zr/SBA-15.

Nitrogen sorption (Figure 1) showed a decrease in the total volume of nitrogen adsorbed with increased loading of Pd, Pt, and Zr, indicating an increase in filling of the pores of the support by added metal compounds. This finding was also reported by Adrover et al. [22]. The pore size distribution chart (Figure 2) shows that adding Pd and Pt to SBA-15 led to the formation of catalysts with bimodal pore size distribution and a maximum size of 3.8 and 5.6 nm. Furthermore, the addition of these two metals narrowed the distribution range of the largest pore size, suggesting filling of the SBA-15 mesopores. It can also be seen that increased Zr content (from 5 to 15 wt%) reduced the overall large pore

size volume (5.6 nm), but at the same time, the smallest pore size volume (3.8 nm) stayed constant for all catalysts with the three components (Pd, Pt, and Zr). Thus, it appears that the metals first filled in the mesopores, obstructing them, and then formed new pores of 3.8 nm. A similar result was obtained by Hassan et al. [23], who showed that a new smaller pore range was formed with increasing content of Co loaded on SBA-15.

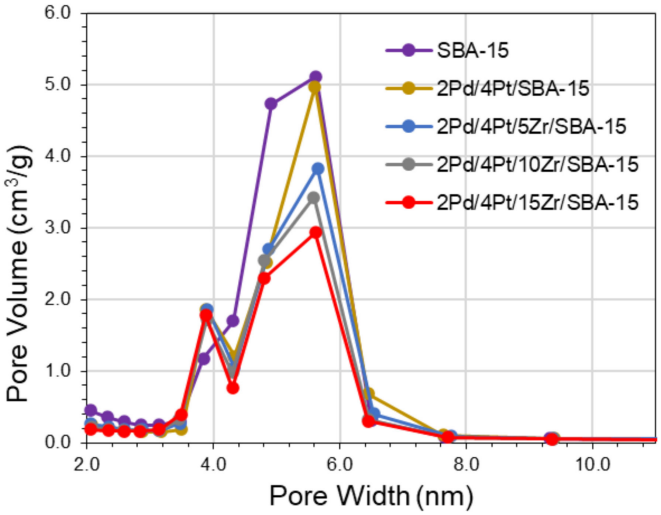

Figure 2. Pore volume versus pore width for 2Pd/4Pt/xZr/SBA-15.

Table 2 lists the structural properties of the catalysts. The surface area decreased as the loading of metal increased, from 836 m^2/g for pure SBA-15 to 432 m^2/g for 2Pd/4Pt/15Zr/SBA-15. As expected, the pore volume also decreased, from 0.82 cm^3/g for SBA-15 to 0.59 cm^3/g for 2Pd/4Pt/15Zr/SBA-15, confirming that the three metals indeed filled the SBA-15 pores.

Table 2. Textural properties of 2Pd/4Pt/xZr/SBA-15 catalysts.

Catalyst Name	BET Surface Area (SA) (m^2/g)	Pore Volume [a] (cm^3/g)	Pore Size [b] (nm)		Crystallite Size from XRD (nm)	
			Small	Large	PdO	Pt
SBA-15	836	0.82	NA	5.6	NA	NA
2Pd/4Pt	608	0.72	3.8	5.6	7.2	33.1
2Pd/4Pt/5Zr	554	0.64	3.8	5.6	9.7	37.4
2Pd/4Pt/10Zr	483	0.59	3.8	5.6	9.3	43.9
2Pd/4Pt/15Zr	432	0.54	3.8	5.6	11.2	43.7

[a] BJH desorption total pore volume; [b] BJH desorption average pore size; NA—not applicable.

2.3. XRD Analysis

Figure 3 shows the diffractograms of 2Pd/4Pt/xZr/SBA-15 catalysts with and without Zr. The amorphous portion of SBA-15 was found between 20 and 30° 2θ. In the samples with 10 and 15 wt% Zr, tetragonal zirconia was the major phase, as indicated by a characteristic peak at 2θ = 30.2°, which corresponds to the (111) reflection, and peaks at 50.3° and 60.0°, which are the (220) and (311) reflections, related to tetragonal zirconia (PDF 01-070-8758). These lines cannot be seen in the sample containing 5% Zr because the low amount of zirconia cannot be detected by XRD. However, it was expected that tetragonal zirconia would be the major phase in this sample, since it was prepared under the same conditions as the other two.

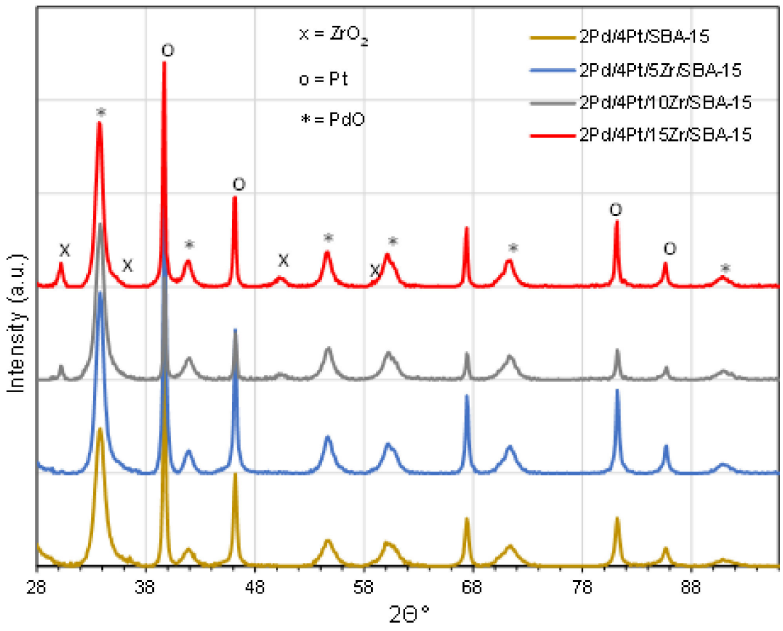

Figure 3. XRD of 2Pd/4Pt/xZr-SBA-15 catalysts.

For all catalysts, metallic face centered cubic platinum Pt was identified with peaks at 2θ = 39.7°, 46.2°, 67.4°, and 82.3°, corresponding to the (111), (200), (220), and (311) reflections, respectively [24]. PdO appeared to be the only Pd phase in all catalysts, as indicated by the (101) and (110) reflections at 2θ = 33.8° and 42.0°, and all reflections for pure Pd were not detected. In all samples, there was no indication of a Pd–Pt alloy, which typically forms when both Pt and Pd are added to a support and calcined. The formation of this alloy is dependent on the calcination conditions. For example, a calcination temperature as low as 300 °C for the formation of the alloy has been reported in the literature. However, the alloy was formed only after reduction with hydrogen [25]. On the other hand, other authors have indicated that temperatures above 500 °C are required to form the Pd–Pt alloy. In the current study, the main reflections of the Pd–Pt alloy of (111) at 2θ = 39.97°, (200) at 2θ = 46.49, and (220) at 2θ = 67.86° were not detected in any diffractograms of the catalysts. Overall, the XRD results suggest that PdO and Pt are separate components and that no alloy is formed under the conditions used for catalyst preparation.

The Sherrer equation was used to calculate particle size, and the values are shown in Table 2. The crystallite size of Pt was found to be larger than that of PdO overall, and this may be due to its higher concentration and the extra calcination step after loading Pd, both of which favor particle sintering. Furthermore, it can be seen that the Pt particles increased in size with Zr content.

2.4. XPS Analysis

XPS analysis was performed on fresh Pd–Pt catalysts supported on SBA-15 doped with different concentrations of Zr. Figure 4 shows the Pd 3d XPS spectra of the three fresh catalysts of the series. The analysis of peak Gaussian fitting revealed the presence of three Pd $3d_{5/2}$ peaks at BE between 334.50 and 334.52, 335.9 and 336.09, and 338.03 and 338.45 eV and three Pd $3d_{3/2}$ peaks at BE between 339.79 and 340.81, 341.19 and 341.30, and 343.32 and 343.74 eV, which can be assigned to Pd^0, Pd^{2+}, and Pd^{4+} species, respectively (Figure 4). The relative concentrations of the Pd in the three oxidation states obtained from deconvolution of the XPS spectra are shown in Table 3. It was found that the surface content of each Pd species was similar for the three catalysts and was composed mostly of Pd^{2+} (80–85%) and Pd^{4+} (13–16%), with a small amount of metallic Pd (3–5%). Overlapping Zr 3p peaks with Pd 3d were found at 350–345 and 335–325 eV. As expected, their peak height rose proportionally with the increasing amount of Zr in the catalysts.

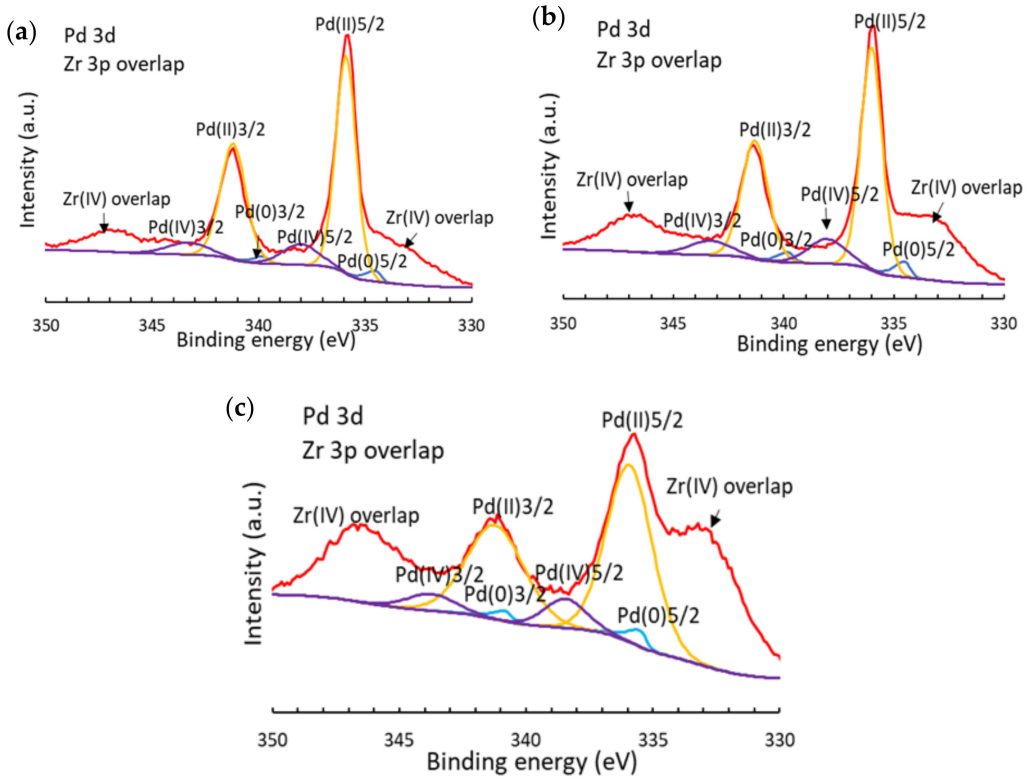

Figure 4. Peak fit analysis of overlapping Pd 3d and Zr(II) 3p XPS spectra of: (**a**) 2Pd/4Pt/5Zr/SBA-15, (**b**) 2Pd/4Pt/10Zr/SBA-15, and (**c**) 2Pd/4Pt/15Zr/SBA-15.

Table 3. Relative intensities of Pd 3d and Pt 4f states from XPS data for 2Pd/4Pt/xZr/SBA-15 catalysts.

Catalyst	Pd 3d (%) [a]			Pt 4f (%) [a]		
	Pd^0	Pd^{2+}	Pd^{4+}	Pt^0	Pt^{2+}	Pt^{4+}
2Pd/4Pt/5Zr	3.6	82.4	14.0	93.8	5.8	0.38
2Pd/4Pt/10Zr	4.8	79.7	15.6	92.3	6.8	ND
2Pd/4Pt/15Zr	3.5	83.9	12.6	27.3	43.6	29.1
2Pd/4Pt/15Zr (aged)	12.4	70.2	17.7	18.3	55.3	26.5

[a] Fraction of each peak over total sum of all peaks obtained by deconvolution; ND—not determined.

The XPS Pt 4f spectra for all catalysts are displayed in Figure 5. The spectra of 2Pd/4Pt/5Zr/SBA-15 and 2Pd/4Pt/10Zr/SBA-15 are very similar. They both show doublets, which were assigned to Pt(0) $4f_{7/2}$ and $4f_{5/2}$ at 71.2 and 74.5 eV, respectively. It can be seen in Table 3 that catalysts containing 5 and 10 wt% Zr had metallic Pt as the dominant species (>90%), with Pt^{2+} accounting for 6–7%, and almost no Pt^{4+} was detected ($\leq$0.38%).

On the other hand, the Pt 4f spectrum of 2Pd/4Pt/15Zr/SBA-15 did not show a well-defined peak shape due to the presence of different amounts of Pt in the three oxidation states. The distribution of the same species in this sample was significantly different, showing 27.3% Pt^0, 43.6% Pt^{2+}, and 29.1% Pt^{4+}. Thus, the XPS analysis revealed that the main difference between the three catalysts was that the highest amount of Pt^{4+} and Pt^{2+} was found in the 2Pd/4Pt/15Zr/SBA-15 sample (43.6% Pt^{2+} and 29.1% Pt^{4+}), compared to less than 7% Pt^{2+} and 0.38% Pt^{4+} in the other two catalysts (Table 3). The role of zirconia and other supports in stabilizing the high-oxidation states of Pt were discussed in previous studies [26,27]. It has been suggested that the mechanism of stabilization is an interaction between Pt and the support, resulting in the formation of new binary oxides composed of platinum and support cations. Based on this, we can presume that Zr plays a determinative

role in the formation and stabilization of Pt in high-oxidation states, and the effect of Zr was the most pronounced with 15 wt% Zr. In a study by Torralba et al. [28], the authors showed that highly oxidized Pt was stabilized by zirconia and enhanced catalytic activity for methane oxidation.

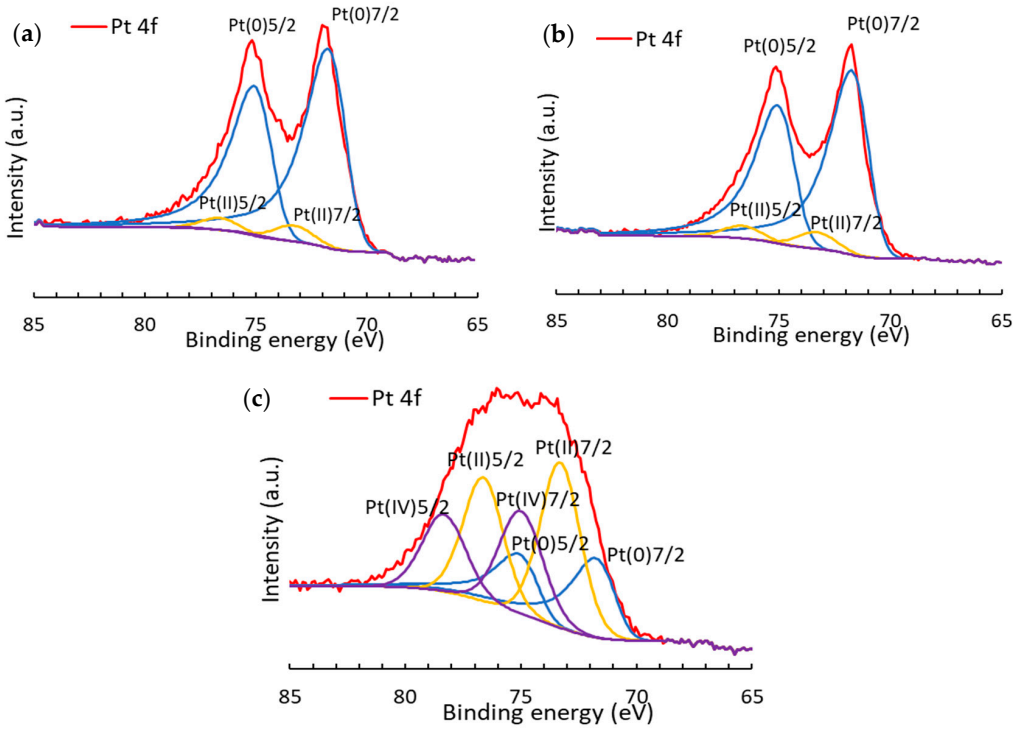

Figure 5. Peak fit analysis of Pt 4f XPS spectra of: (**a**) 2Pd/4Pt/5Zr/SBA-15, (**b**) 2Pd/4Pt/10Zr/SBA-15, and (**c**) 2Pd/4Pt/15Zr/SBA-15.

Furthermore, the XPS Pd 3d scan of the aged 2Pd/4Pt/15Zr showed an increase in Pd(0) compared to the fresh sample (3.5% vs. 12.4% in fresh and aged, respectively). Sulfur can adsorb onto the surface of palladium and reduce Pd(II) to Pd(0), resulting in decreased catalytic activity, which agrees with the results obtained in [29]. On the other hand, under the same conditions, Pt(II) content slightly increased, suggesting oxidation of Pt(0). In summary, the negative effect of Pd on activity is larger than the positive effect of increased Pt(II) content.

2.5. TPR Characterization

The reducibility of the prepared catalysts was characterized by H_2-TPR experiments. To facilitate the identification of TPR peaks, pure SBA-15, zirconia-supported SBA-15, and monometallic Pd or Pt on SBA-15 were tested under the same conditions as 2Pd/4Pt/15Zr/SBA-15. Figure 6 shows the H_2 consumption curves of the prepared samples. Curves a and b (SBA-15 and 15Zr/SBA-15, respectively) show no H_2 consumption peaks, indicating that there was no reduction of the bare or Zr-doped silica supports. As such, the observed hydrogen consumption peaks in the TPR curves of other catalysts correspond to the reduction of supported Pd and Pt. Curve c (4Pt/SBA-15) shows a large H_2 consumption peak centered at 480 °C, which can be attributed to the reduction of PtO_x at high temperature, indicating a strong interaction of Pt with the support [30,31]. When Pt was loaded on the Zr-doped silica (curve d), the TPR profile was markedly different, demonstrating two overlapping peaks centered at 360 and 480 °C, suggesting the existence of weakly and strongly bound PtO_x to the support, respectively [31]. The addition of Zr to silica led to a new reduction peak at low temperature, clearly indicating the involvement of zirconia in the formation of more reducible PtO_x species in the catalyst. This observation agrees with [32], which demonstrated a low-temperature reduction peak at near 325 °C assigned to PtO_x species bound to zirconia.

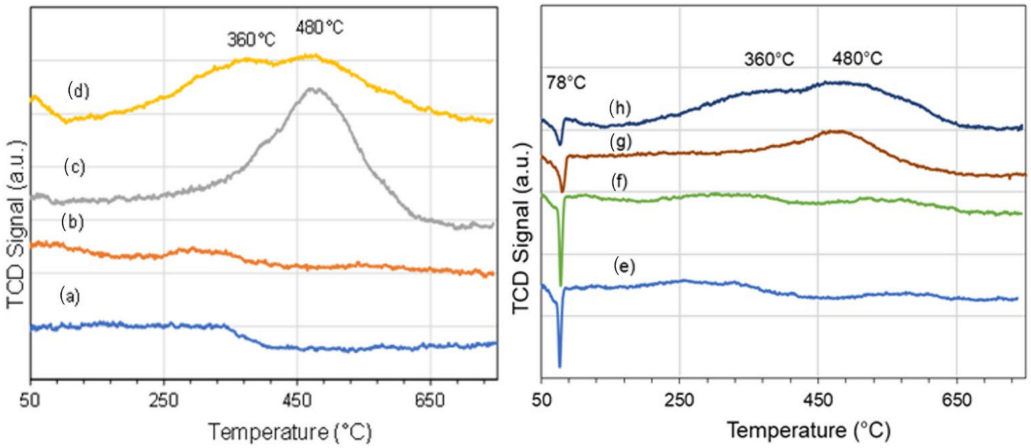

Figure 6. H_2 TPR profiles of Pd–Pt catalysts: (**a**) SBA-15, (**b**) 15Zr/SBA-15, (**c**) 4Pt/SBA-15, (**d**) 4Pt/15Zr/SBA-15, (**e**) 2Pd/SBA-15, (**f**) 2Pd/15Zr/SBA-15, (**g**) 2Pd/4Pt/SBA-15, and (**h**) 2Pd/4Pt/15Zr/SBA-15.

When 2 wt% Pd was loaded on SBA-15 and 15Zr/SBA-15 (curves e and f, respectively), the negative peak at 78 °C indicates the release of H_2 from PdH_x species that formed at lower temperatures [33]. In addition, there was no significant change in the TPR profiles of these catalysts, indicating that Zr addition did not influence the reducibility of Pd in the catalysts.

For the bimetallic Pd–Pt/SBA-15 catalyst without Zr (curve g), the H_2 reduction peak for Pd at 78 °C was significantly reduced, indicating decreased formation of hydrides, which agrees with Radlik and Noh et al. [34,35], who determined that Pt impeded the formation of Pd hydrides. Furthermore, the peak temperatures and shapes in curve g were very similar to the individual peaks found in the TPR profiles of monometallic 4Pt/SBA-15 and 2Pd/15Zr/SBA-15 (curves c and f, respectively). As such, there was no apparent change in the reducibility of Pt and Pd when they were loaded together on the same support to form the bimetallic catalyst. Curve h shows the TPR curve of 2Pd/4Pt/15Zr/SBA-15, which shows no change in the Pd reduction peak. The profile also shows the same two H_2 uptake peaks for Pt at 360 and 480 °C as in curve d (TPR of 4Pt/15Zr/SBA-15), confirming the same effect of zirconia on Pt reducibility irrespective of whether both metals were loaded on the support or not.

Finally, a comparison of the TPR profiles of the three catalysts with varying amounts of dopant (5, 10, and 15 wt% Zr) is shown in Figure 7. All three catalysts exhibited H_2 consumption peaks at 360 and 480 °C, indicating that they all had weakly and strongly bound PtO_x species. Table 4 shows the H_2 uptake of Pt of the three catalysts, and it can be seen that the H_2 quantity increased for Pt associated with a peak at 360 °C with zirconia content from 5 to 15 wt%. This result indicates that zirconia clearly influenced the formation of more reducible PtO_x species, and the amounts of these species correlated with the Zr content. At the same time, there was no noticeable trend in H_2 uptake for the higher temperature peak of 460 °C with Zr content in all three catalysts.

Based on the analysis of TPR data, we can conclude that the additional H_2 consumption peak at a low temperature of 360 °C was a result of the interaction of zirconia with Pt and reflected the increased reducibility of modified vs. unmodified catalysts. Furthermore, the H_2 uptake at the 360 °C peak was the highest for the 2Pd/4Pt/15Zr/SBA-15 catalyst, correlating with the largest amount of interacting interface between Pt and ZrO_2. The better reducibility of Pt in close proximity to zirconia could make its bonding of hydrogen and methane and the sequential breaking of the C-H bond easier, which is the rate-limiting step in the oxidation of methane [36]. Taking this into consideration, we can suppose that 2Pd/4Pt/15Zr/SBA-15 would be the most active catalyst for methane oxidation.

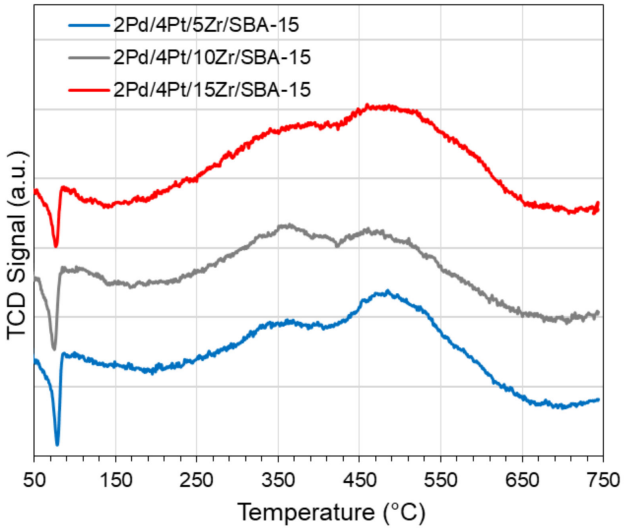

Figure 7. H_2-TPR profiles of 2Pd/4Pt/xZr/SBA-15 catalysts.

Table 4. H_2-TPR hydrogen uptake of 2Pd/4Pt/xZr/SBA-15 catalysts.

Catalyst	Total H_2 Consumption (mmol H_2/g Catalyst) at TPR Peak Maxima	
	360 °C	**480 °C**
2Pd/4Pt/5Zr	0.10	0.22
2Pd/4Pt/10Zr	0.12	0.14
2Pd/4Pt/15Zr	0.17	0.27

2.6. Catalytic Activity Tests

The effect of adding Zr to Pd–Pt-SBA-15 catalysts on methane oxidation activity was studied in a fixed-bed reactor using simulated NG exhaust. The fresh catalysts were tested, and their gradient runs are shown in Figure 8. When fresh, the catalyst without Zr (2Pd/4Pt/SBA-15) showed the lowest activity in terms of the highest T_{50}, but it was similar to the one containing 5 wt% Zr. Furthermore, an increase in activity was observed when the Zr content was increased to 10 and 15 wt% compared to the catalysts with 0 and 5 wt% Zr.

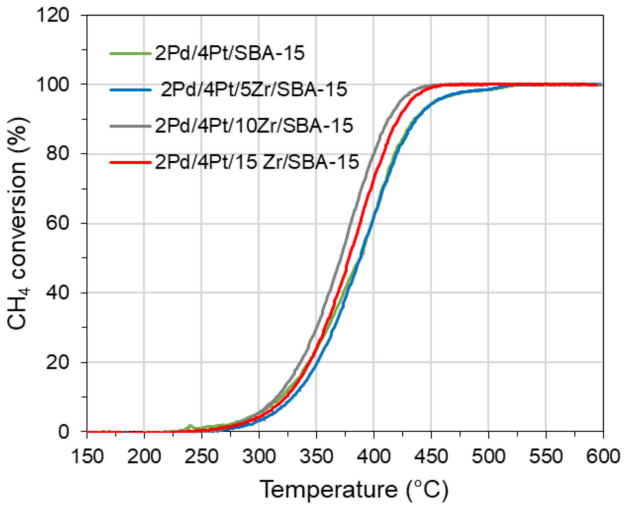

Figure 8. Gradient runs of fresh 2Pd/4Pt/xZr-SBA-15 catalysts. Feed gas composition: 1 vol% CH_4, 10 vol% O_2, 6 vol% CO_2, 10 ppm SO_2, and 10 vol% H_2O in a balance of N_2. WTSV: 0.0601 g s/cm^3.

The catalysts were then aged for 40 h at 500 °C using simulated lean burn NG exhaust, which included water vapor and sulfur dioxide. Figure 9 shows the changes of CH_4 conversion with time during aging. The curves for all catalysts show a sudden drop in conversion at the initial stage, which can be explained by the strong adsorption of SO_2 on the active metal sites decreasing their activity for methane oxidation. After approximately 20 min, the catalysts with 10 and 15 wt% Zr demonstrated almost no decrease in methane conversion, suggesting that the continued sulfur adsorption on the zirconia protected the remaining active sites from being blocked. For example, the methane conversion of 2Pd/4Pt/15Zr/SBA-15 was at 88% at the beginning of the aging procedure, then dropped to 60% in the first 20 min and stayed constant at this value for 40 h. The same tendency was found for 2Pd/4Pt/10Zr/SBA-15, showing an initial CH_4 conversion near 83% and then dropping to 60% after one hour, with a slight reduction in conversion near 55% after 40 h. On other hand, the catalysts with no Zr (2Pd/4Pt/SBA-15) exhibited only 55% CH_4 conversion at the starting point, then reduced to 30% conversion after 40 h. The catalyst that contained 5 wt% Zr showed slightly better performance than 2Pd/4Pt/SBA-15 throughout the aging process (~3% higher CH_4 conversion) due to the presence of Zr.

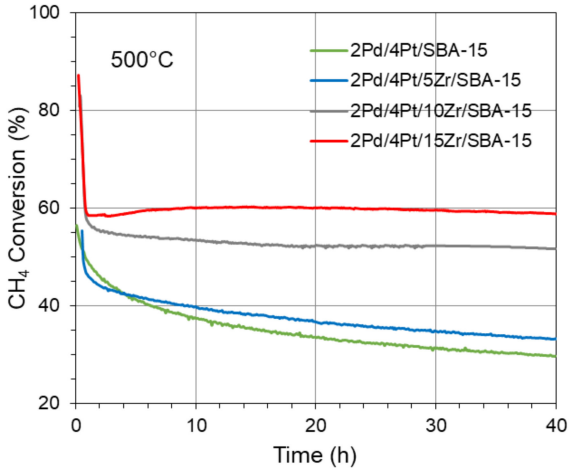

Figure 9. Conversion of methane over 2Pd/4Pt/xZr/SBA-15 catalysts during aging at 500 °C. Feed gas composition: 1 vol% CH_4, 10 vol% O_2, 6 vol% CO_2, 10 ppm SO_2, and 10 vol% H_2O in a balance of N_2. WTSV: 0.0601 g s/cm^3.

The aged catalysts were further evaluated for methane oxidation activity with gradient runs to determine their T_{50}. Figure 10 shows the light-off curves of catalysts after aging, and Table 5 presents a comparison of T_{50} values between fresh and aged catalysts. The curve for 2Pd4Pt/SBA-15 shows an extensive loss of activity, as the catalyst did not even reach 100% methane conversion at 600 °C. Furthermore, it exhibits a T_{50} of 581 °C, with a difference of 194 °C between fresh and aged catalysts, indicating low stability. On the other hand, the Zr-containing catalysts had much lower T_{50}, between 481 and 502 °C, and a much smaller difference in T_{50} (less than 121 °C) between fresh and aged, confirming the better stability of the modified catalysts.

From the literature [18], it is known that Pd catalysts with sulfatable supports, such as zirconia and alumina, are more resistant to sulfur poisoning because the support acts as a trap for the sulfur species, thereby protecting Pd active sites from poisoning. Since SBA-15 is a silica support, it is non-sulfating, and the active metals can be easily deactivated by sulfur. When Zr was added to SBA-15, the catalysts became more active and stable. This is well demonstrated by the activity of 2Pd/4Pt/SBA-15, which was lower in comparison to the three modified catalysts. Thus, the overall activity and aging results suggest that Zr on silica acts as a sulfur sink and prevents the sulfur poisoning of Pd and Pt, which enhances catalyst activity and stability.

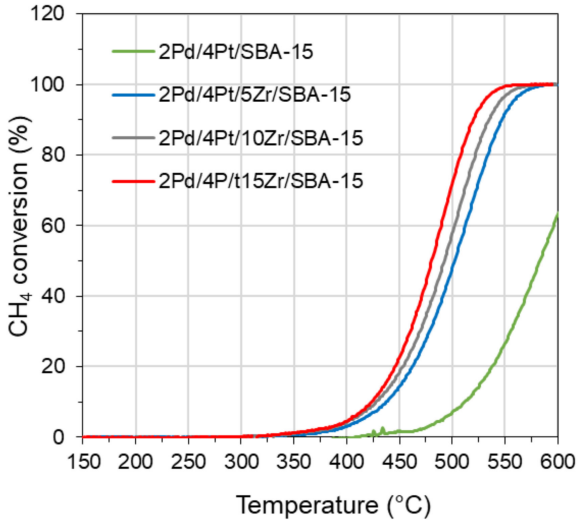

Figure 10. Gradient runs of 2Pd/4Pt/xZr/SBA-15 catalysts after aging. Feed gas composition: 1 vol% CH_4, 10 vol% O_2, 6 vol% CO_2, 10 ppm SO_2, and 10 vol% H_2O in a balance of N_2. WTSV: 0.0601 g s/cm^3.

Table 5. T_{50} results of fresh and aged 2Pd/4Pt/xZr/SBA-15 catalysts.

Catalyst Name	T_{50} (°C)		Difference
	Fresh	Aged	
2Pd/4Pt	389	583	194
2Pd/4Pt/5Zr	389	502	113
2Pd/4Pt/10Zr	371	492	121
2Pd/4Pt/15Zr	378	481	103

The graph in Figure 11 provides some insight into the poisoning effect of sulfur on the catalysts. The graph shows the concentration of SO_2 at the outlet of the reactor, which was measured during the gradient runs after aging. The least active catalyst of the series, 2Pd/4Pt/SBA-15, showed no major change with the initial SO_2 concentration of 12 ppm during the run until around 400 °C, when the concentration decreased significantly. SBA-15, as a non-sulfating silica support, did not bond with sulfur at lower temperatures and the outlet SO_2 concentration was not affected. As the temperature increased, the SO_2 concentration decreased, suggesting that SO_2 was trapped on the Pd surface, thus poisoning the catalyst and reducing its activity. On the contrary, the catalysts with Zr all exhibited low SO_2 concentrations of 2–4 ppm at the beginning of the gradient runs, suggesting that the sulfur bound immediately to the zirconium sulfating support. The catalysts with 10 and 15 wt% Zr, which were the most active of the series, had the lowest concentrations of SO_2 at the beginning of the gradient runs, indicating that more SO_2 was bound on their surface, thus protecting the Pd. As the temperature increased, the concentration of SO_2 increased slightly, suggesting a partial release of the bound sulfur from the catalyst.

Additionally, according to the XPS data, 2Pd/4Pt/15Zr demonstrated the highest content of Pt^{2+} and Pt^{4+}. This may be another reason for the high activity of this catalyst, as these Pt electric dipole sites exert a strong polarization effect on CH_4 molecules. This polarization causes a weakening of the C-H bond, which in turn facilitates the removal of the first hydrogen atom from the adsorbed methane molecule, which represents the rate-limiting step in the oxidation process [28]. These results clearly show that zirconia and platinum play an important role in the catalyst activity, stability, and resistance to sulfur poisoning of methane oxidation catalysts.

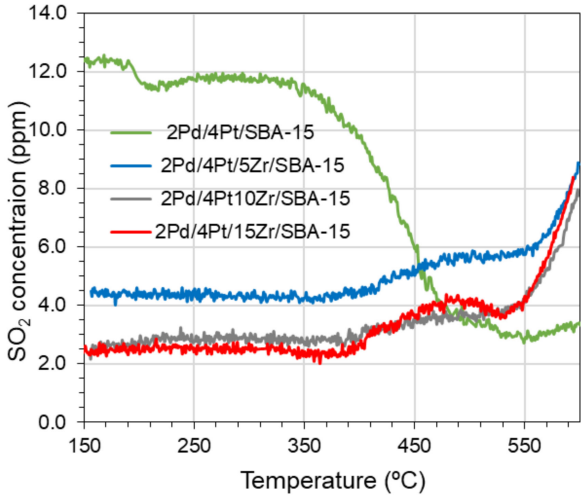

Figure 11. SO_2 concentration during gradient runs of aged 2Pd/4Pt/xZr/SBA-15 catalysts.

3. Materials and Methods

3.1. Support and Catalyst Preparation

A workflow of the catalyst preparation is presented in Figure 12 to better understand the multistep synthesis of the catalytic materials used in this study.

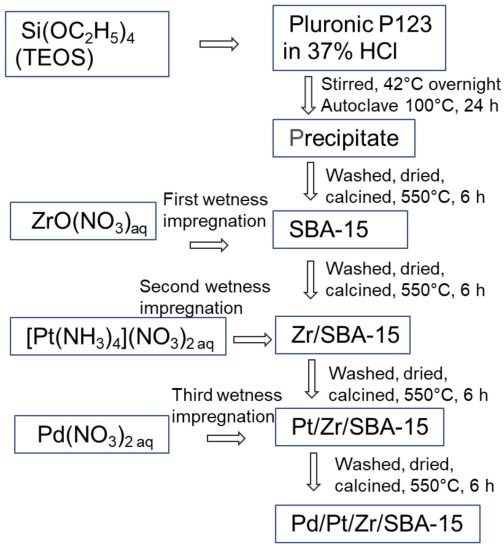

Figure 12. Workflow of catalyst preparation.

The preparation of the mesoporous catalyst support SBA-15 followed the procedure of Zhao et al. [37]. The synthesis involved first dissolving 8.16 g of Pluronic P123 (Sigma Aldrich Co., Oakville, ON, Canada) in 4.40 g of 37% HCl and stirring at 42 °C overnight. Next, 16 g of tetraethylorthosilicate (Sigma Aldrich Co., Oakville, ON, Canada) was added to the solution dropwise using a burette. After that, the solution was left to stir for 24 h on low heat. The solution was then placed in an autoclave at 100 °C for 24 h. The product was washed 15 times using 1 L of DI water each time, for a total of 15 L. Finally, the sample was dried at 120 °C for 4 h and then calcined at 550 °C for 6 h.

Zirconium was loaded on SBA-15 support by incipient wetness impregnation with an aqueous solution of zirconium(IV) oxynitrate hydrate (Sigma Aldrich Co., Oakville, ON, Canada) to obtain 5, 10, and 15 wt% Zr, followed by drying at 120 °C overnight and calcination at 550 °C for 6 h. Aqueous solutions of palladium and platinum precursors (palladium(II) nitrate and tetraammineplatinum(II) nitrate; Alfa Aesar, Tewksbury, MA,

USA) were added sequentially to the modified SBA-15 by incipient wetness impregnation with drying (120 °C for ~16 h) and calcination (550 °C for 6 h) steps between metal loading. The produced catalysts had 2 wt% Pd and 4 wt% Pt.

The final catalysts were denoted as 2Pd/4Pt/xZr/SBA-15, where x is the nominal wt% of Zr loaded on SBA-15.

3.2. Characterization of Catalysts

Catalyst composition was determined using flame atomic absorption (FAA; Agilent, Mississauga, ON, Canada) and SEM. A Hitachi S3400N VP-SEM (Hitachi Ltd., Tokyo, Japan) was used for SEM with an Oxford INCA energy-dispersive X-ray (EDX) detector system (Oxford Instruments, Oxfordshire, UK) operating at 20 kV and 80–90 mA. A thin layer of powder catalyst was deposited and held in place on a double-sided carbon tape. The excess was blown off with a gentle stream of nitrogen. For each catalyst, 10 random locations chosen by the INCA automation software (Oxford Instruments, Inca for Windows version 5.05, Issue 21b SP3) were analyzed. The average and standard deviation of the measurements were calculated to determine the final composition of the catalysts. The FAA procedure involved fusing the catalysts using sodium peroxide at approximately 700 °C. The melt was dissolved in water and acidified with HCl. Tellurium was added, followed by stannous chloride for precipitation. The tellurium and precious metal precipitate were filtered out of the solution and dissolved in aqua regia. The dissolved samples were analyzed using a flame atomic absorption spectrometer.

The textural properties of the catalysts, including pore size, pore volume, and specific surface area, were measured by the N_2 adsorption method using an ASAP2010 instrument (Micromeritics Inc., Norcross, GA, USA). The samples were degassed at 250 °C for 5 h and N_2 adsorption was carried out at 77 K. Pore size and pore volume were calculated using the desorption branch of the N_2 adsorption/desorption isotherm by the BJH method.

X-ray powder diffraction (XRD) patterns were recorded by Rigaku Ultima IV XRD spectrometer (Tokyo, Japan) over the angular range of 5–95° 2θ in steps of 0.02°. The XRD system was operated in the θ:θ geometry employing Cu K radiation (λ = 1.5405981 Å) and was equipped with a diffracted-beam graphite monochromator, a scintillation detector, and solid-state counting electronics. XRD data were processed using Jade Plus version 7.5 software. The average crystallite size was calculated based on the Scherrer equation using the Rigaku PDXL Diffraction software's (MDI JADE, V8.3@2021-07-06) whole pattern profile fitting program (WPPF).

For the XPS analysis, the samples were analyzed as received using the Kratos Axis Ultra XPS device (Kratos Analytical, Manchester, UK) equipped with a monochromated Al X-ray source. Three wide-area scans of each sample were performed to confirm uniformity, and then three high-resolution scans of each element detected were taken. The high-resolution spectra of identical positioning and width were summed to improve the signal-to-noise ratio. Analyses were carried out using an accelerating voltage of 15 kV and a current of 12 mA. The analysis area was 300 × 700 µm. Charge build-up was compensated by using the Axis charge balancing system. The pressure in the analysis chamber during the analysis of the entire dataset was at $9.6 \times 10^{-10} \pm 0.3 \times 10^{-10}$ torr. XPS is a technique that provides chemical state information from the top 3–7 nm of a sample. Wide-area scans were performed at a pass energy of 160 eV, while high-resolution scans were carried out at a pass energy of 20 eV. Peak assignments were based on the NIST database (http://srdata.nist.gov/xps/Bind_E.asp, accessed on 9 May 2023) and relevant publications. Peak fitting was performed using CasaXPS (v. 2.3.22PR1.0) data processing software. Shirley background correction procedures were used for all fits, as provided by CasaXPS. Following best practices, the curve-fitting procedures used for high-resolution spectra presented in this report used a Gaussian–Lorentzian (30) function, with the following notable exceptions: Pd metals used an LA (1.9,7,2) function, Pt metals, an LA (1.2,85,70) function, and SiO_2, an LA (4.2,9,4) function. High-resolution analysis was calibrated to an adventitious C 1s signal at 284.8 eV. Quantification was performed using sensitivity factors provided by the KratosPlus element library of CasaXPS.

A Micromeritics AutoChem II 2920 Analyzer (Micromeritics, Norcross, GA, USA) equipped with a thermal conductivity detector was used for H2-TPR studies. The catalyst (50 ± 3 mg) was pretreated in He flow of 30 mL min^{-1} at 300 °C for 30 min. The sample was then cooled to room temperature in the same He flow. The H_2-TPR profile was obtained when the catalyst was heated to 900 °C at a heating rate of 10 °C min^{-1} in a 50 mL min^{-1} flow of 10 vol% H_2 and balance argon gas mixture.

3.3. Catalyst Activity

The catalysts were tested in a fixed-bed flow reactor system built in house consisting of a vertical quartz tube reactor (6.12 mm nominal ID by 40.64 cm long) enclosed in a temperature-controlled furnace. Each sample was pelletized and sieved to a particle size of 125–180 μm prior to testing. The particles (~500 mg) were then loaded into a reactor yielding a typical catalyst bed height of 26 mm. All catalytic experiments were conducted at a weight-time space velocity (WTSV) of 0.0601 g s/cm^3 (standardized to 20 °C and 1 atm). To evaluate the performance of a fresh and aged catalyst, temperature gradient runs (light-off) were used, which involved raising the furnace temperature from 75 to 600 °C at 3 °C/min. The feed gas composition simulated a lean burn NG engine exhaust and consisted of 1 vol% CH_4, 10 vol% O_2, 6 vol% CO_2, 10 ppm SO_2, and 10 vol% H_2O in a balance of N_2 supplied at 500 mL/min. The catalysts were aged using an isothermal temperature of 500 °C for 40 h using the same gas composition.

4. Conclusions

SBA-15 was doped with various amounts of zirconia (5, 10, and 15 wt%) and impregnated with Pd and Pt (2 and 4 wt%, respectively). XRD analysis revealed that the catalyst contained individual PdO and Pt particles with apparently no alloy formation between Pd and Pt and identified a tetragonal zirconia phase. Among the series of catalysts, the 2Pd/4Pt/15Zr/SBA-15 catalyst, with the highest Zr concentration of 15 wt%, was the most active, stable, and sulfur resistant, as demonstrated by the lowest T_{50} of 481 °C after 40 h of aging. The increased performance and stability of this catalyst was attributed to the higher content of reducible Pt species as well as the Zr trapping capacity of sulfur, which provides protection for the active metals. The results of this study indicate that 2Pd/4Pt/15Zr/SBA-15 catalyst may be a good candidate for practical application in reducing methane slip from lean burn natural gas engines.

Author Contributions: Conceptualization, G.C.; methodology, G.C. and L.N.; validation, G.C. and L.N.; formal analysis, G.C. and L.N.; data curation, G.C. and M.T.; writing—original draft preparation, G.C.; writing—review and editing, G.C. and L.N.; visualization, L.N.; supervision, G.C.; project administration, G.C.; funding acquisition, G.C. All authors have read and agreed to the published version of the manuscript.

Funding: This research was funded by Natural Resources Canada through the Program of Energy Research and Development (PERD).

Data Availability Statement: All data generated or analyzed during this study are included in this article.

Acknowledgments: The authors would like to thank Philip Sutherland for catalyst synthesis and characterization and Ray Burich for catalyst performance evaluation.

Conflicts of Interest: The authors declare no conflict of interest.

References

1. Tajima, H.; Tsuru, D. Reduction of Methane Slip from Gas Engines by O_2 Concentration Control Using Gas Permeation Membrane. In *Proceedings of the SAE Technical Paper*; SAE International: Warrendale, PA, USA, 2013.
2. Johnson, J. Methane's Role in Climate Change. *Chem. Eng. News* **2014**, *92*, 10–15. [CrossRef]
3. He, L.; Fan, Y.; Bellettre, J.; Yue, J.; Luo, L. A Review on Catalytic Methane Combustion at Low Temperatures: Catalysts, Mechanisms, Reaction Conditions and Reactor Designs. *Renew. Sustain. Energy Rev.* **2020**, *119*, 109589. [CrossRef]

4. Gélin, P.; Urfels, L.; Primet, M.; Tena, E. Complete Oxidation of Methane at Low Temperature over Pt and Pd Catalysts for the Abatement of Lean-Burn Natural Gas Fuelled Vehicles Emissions: Influence of Water and Sulphur Containing Compounds. *Catal. Today* **2003**, *83*, 45–57. [CrossRef]
5. Li, Z.; Hoflund, G. A Review on Complete Oxidation of Methane at Low Temperatures. *J. Nat. Gas Chem.* **2003**, *12*, 153–160.
6. Fraga, M.A.; Soares de Souza, E.; Villain, F.; Appel, L.G. Addition of La and Sn to Alumina-Supported Pd Catalysts for Methane Combustion. *Appl. Catal. A Gen.* **2004**, *259*, 57–63. [CrossRef]
7. Yasuda, K.; Masui, T.; Miyamoto, T.; Imanaka, N. Catalytic Combustion of Methane over Pt and PdO-Supported CeO_2–ZrO_2–Bi_2O_3/γ-Al_2O_3 Catalysts. *J. Mater. Sci.* **2011**, *46*, 4046–4052. [CrossRef]
8. Barrera, A.; Fuentes, S.; Díaz, G.; Gómez-Cortés, A.; Tzompantzi, F.; Molina, J.C. Methane Oxidation over Pd Catalysts Supported on Binary Al_2O_3–La_2O_3 Oxides Prepared by the Sol–Gel Method. *Fuel* **2012**, *93*, 136–141. [CrossRef]
9. Ziaei-Azad, H.; Khodadadi, A.; Esmaeilnejad-Ahranjani, P.; Mortazavi, Y. Effects of Pd on Enhancement of Oxidation Activity of $LaBO_3$ (B = Mn, Fe, Co and Ni) Pervoskite Catalysts for Pollution Abatement from Natural Gas Fueled Vehicles. *Appl. Catal. B Environ.* **2011**, *102*, 62–70. [CrossRef]
10. Jiang, D.; Khivantsev, K.; Wang, Y. Low-Temperature Methane Oxidation for Efficient Emission Control in Natural Gas Vehicles: Pd and Beyond. *ACS Catal.* **2020**, *10*, 14304–14314. [CrossRef]
11. Corro, G.; Cano, C.; Fierro, J.L.G. A Study of Pt–Pd/γ-Al_2O_3 Catalysts for Methane Oxidation Resistant to Deactivation by Sulfur Poisoning. *J. Mol. Catal. A Chem.* **2010**, *315*, 35–42. [CrossRef]
12. Gholami, R.; Alyani, M.; Smith, K. Deactivation of Pd Catalysts by Water during Low Temperature Methane Oxidation Relevant to Natural Gas Vehicle Converters. *Catalysts* **2015**, *5*, 561–594. [CrossRef]
13. Araya, P.; Guerrero, S.; Robertson, J.; Gracia, F.J. Methane Combustion over Pd/SiO_2 Catalysts with Different Degrees of Hydrophobicity. *Appl. Catal. A Gen.* **2005**, *283*, 225–233. [CrossRef]
14. Okumura, K.; Shinohara, E.; Niwa, M. Pd Loaded on High Silica Beta Support Active for the Total Oxidation of Diluted Methane in the Presence of Water Vapor. *Catal. Today* **2006**, *117*, 577–583. [CrossRef]
15. Yuranov, I.; Moeckli, P.; Suvorova, E.; Buffat, P.; Kiwi-Minsker, L.; Renken, A. Pd/SiO_2 Catalysts: Synthesis of Pd Nanoparticles with the Controlled Size in Mesoporous Silicas. *J. Mol. Catal. A Chem.* **2003**, *192*, 239–251. [CrossRef]
16. Yashnik, S.A.; Chesalov, Y.A.; Ishchenko, A.V.; Kaichev, V.V.; Ismagilov, Z.R. Effect of Pt Addition on Sulfur Dioxide and Water Vapor Tolerance of Pd-Mn-Hexaaluminate Catalysts for High-Temperature Oxidation of Methane. *Appl. Catal. B Environ.* **2017**, *204*, 89–106. [CrossRef]
17. Venezia, A.M.; Di Carlo, G.; Liotta, L.F.; Pantaleo, G.; Kantcheva, M. Effect of Ti(IV) Loading on CH_4 Oxidation Activity and SO_2 Tolerance of Pd Catalysts Supported on Silica SBA-15 and HMS. *Appl. Catal. B Environ.* **2011**, *106*, 529–539. [CrossRef]
18. Escandón, L.S.; Ordóñez, S.; Vega, A.; Díez, F.V. Sulphur Poisoning of Palladium Catalysts Used for Methane Combustion: Effect of the Support. *J. Hazard. Mater.* **2008**, *153*, 742–750. [CrossRef]
19. Velin, P.; Florén, C.R.; Skoglundh, M.; Raj, A.; Thompsett, D.; Smedler, G.; Carlsson, P.A. Palladium Dispersion Effects on Wet Methane Oxidation Kinetics. *Catal. Sci. Technol.* **2020**, *10*, 5460–5469. [CrossRef]
20. Huang, Z.D.; Bensch, W.; Kienle, L.; Fuentes, S.; Alonso, G.; Ornelas, C. SBA-15 as Support for MoS_2 and Co-MoS_2 Catalysts Derived from Thiomolybdate Complexes in the Reaction of HDS of DBT. *Catal. Lett.* **2008**, *122*, 57–67. [CrossRef]
21. Gonzalez, G.; Sagarzazu, A.; Cordova, A.; Gomes, M.E.; Salas, J.; Contreras, L.; Noris-Suarez, K.; Lascano, L. Comparative Study of Two Silica Mesoporous Materials (SBA-16 and SBA-15) Modified with a Hydroxyapatite Layer for Clindamycin Controlled Delivery. *Microporous Mesoporous Mater.* **2018**, *256*, 251–265. [CrossRef]
22. Esperanza Adrover, M.; Pedernera, M.; Bonne, M.; Lebeau, B.; Bucalá, V.; Gallo, L. Synthesis and Characterization of Mesoporous SBA-15 and SBA-16 as Carriers to Improve Albendazole Dissolution Rate. *Saudi Pharm. J.* **2020**, *28*, 15–24. [CrossRef] [PubMed]
23. El Hassan, N.; Aouad, S.; Casale, S.; El Zakhem, H.; El Nakat, H. Oxidation of Carbon Black, Propene and Toluene on Highly Reducible Co/SBA-15 Catalysts. *Comptes Rendus Chim.* **2014**, *17*, 913–919. [CrossRef]
24. Wang, W.; Wang, Z.; Wang, J.; Zhong, C.J.; Liu, C.J. Highly Active and Stable Pt–Pd Alloy Catalysts Synthesized by Room-Temperature Electron Reduction for Oxygen Reduction Reaction. *Adv. Sci.* **2017**, *4*, 1600486. [CrossRef] [PubMed]
25. Morlang, A.; Neuhausen, U.; Klementiev, K.V.; Schütze, F.W.; Miehe, G.; Fuess, H.; Lox, E.S. Bimetallic Pt/Pd Diesel Oxidation Catalysts: Structural Characterisation and Catalytic Behaviour. *Appl. Catal. B Environ.* **2005**, *60*, 191–199. [CrossRef]
26. Nagai, Y.; Hirabayashi, T.; Dohmae, K.; Takagi, N.; Minami, T.; Shinjoh, H.; Matsumoto, S. Sintering Inhibition Mechanism of Platinum Supported on Ceria-Based Oxide and Pt-Oxide-Support Interaction. *J. Catal.* **2006**, *242*, 103–109. [CrossRef]
27. Yazawa, Y.; Yoshida, H.; Komai, S.I.; Hattori, T. The Additive Effect on Propane Combustion over Platinum Catalyst: Control of the Oxidation-Resistance of Platinum by the Electronegativity of Additives. *Appl. Catal. A Gen.* **2002**, *233*, 113–124. [CrossRef]
28. Torralba, R.; Corro, G.; Rosales, F.; Bañuelos, F.; Pal, U.; Olivares-Xometl, O.; Guilleminot, E.; Fierro, J.L.G. Total Oxidation of Methane over Sulfur Poisoning Resistant Pt/ZrO_2 Catalyst: Effect of Pt^{2+}–Pt^{4+} and Pt^{2+}–Zr^{4+} Dipoles at Metal-Support Interface. *Catal. Lett.* **2021**, *151*, 1592–1603. [CrossRef]
29. Monai, M.; Montini, T.; Melchionna, M.; Duchoň, T.; Kúš, P.; Chen, C.; Tsud, N.; Nasi, L.; Prince, K.C.; Veltruská, K.; et al. The Effect of Sulfur Dioxide on the Activity of Hierarchical Pd-Based Catalysts in Methane Combustion. *Appl. Catal. B Environ.* **2017**, *202*, 72–83. [CrossRef]

30. Rodríguez-Castellón, E.; Mérida-Robles, J.; Díaz, L.; Maireles-Torres, P.; Jones, D.J.; Rozière, J.; Jiménez-López, A. Hydrogenation and Ring Opening of Tetralin on Noble Metal Supported on Zirconium Doped Mesoporous Silica Catalysts. *Appl. Catal. A Gen.* **2004**, *260*, 9–18. [CrossRef]
31. Bhogeswararao, S.; Srinivas, D. Catalytic Conversion of Furfural to Industrial Chemicals over Supported Pt and Pd Catalysts. *J. Catal.* **2015**, *327*, 65–77. [CrossRef]
32. Tang, Z.; Liu, P.; Cao, H.; Bals, S.; Heeres, H.J.; Pescarmona, P.P. Pt/ZrO_2 Prepared by Atomic Trapping: An Efficient Catalyst for the Conversion of Glycerol to Lactic Acid with Concomitant Transfer Hydrogenation of Cyclohexene. *ACS Catal.* **2019**, *9*, 9953–9963. [CrossRef]
33. Howeizi, J.; Taghvaei-Ganjali, S.; Malekzadeh, M.; Motiee, F.; Sahebdelfar, S. Effect of the Distribution and Dispersion of Palladium Nanoparticles on the Reducibility and Performance of Pd/Al_2O_3 Catalyst in Liquid-Phase Hydrogenation of Olefins. *React. Kinet. Mech. Catal.* **2020**, *130*, 777–795. [CrossRef]
34. Radlik, M.; Śrębowata, A.; Juszczyk, W.; Matus, K.; Małolepszy, A.; Karpiński, Z. N-Hexane Conversion on γ-Alumina Supported Palladium–Platinum Catalysts. *Adsorption* **2019**, *25*, 843–853. [CrossRef]
35. Noh, H.; Flanagan, T.B.; Sonoda, T.; Sakamoto, Y. Solubility and Thermodynamics of Hydrogen in Homogeneous f.c.c. PdPt Alloys. *J. Alloys Compd.* **1995**, *228*, 164–171. [CrossRef]
36. Corro, G.; Torralba, R.; Pal, U.; Olivares-Xometl, O.; Fierro, J.L.G. Total Oxidation of Methane over Pt/Cr_2O_3 Catalyst at Low Temperature: Effect of Pt0–Ptx+ Dipoles at the Metal–Support Interface. *J. Phys. Chem. C* **2019**, *123*, 2882–2893. [CrossRef]
37. Zhao, D.; Huo, Q.; Feng, J.; Chmelka, B.F.; Stucky, G.D. Nonionic Triblock and Star Diblock Copolymer and Oligomeric Sufactant Syntheses of Highly Ordered, Hydrothermally Stable, Mesoporous Silica Structures. *J. Am. Chem. Soc.* **1998**, *120*, 6024–6036. [CrossRef]